IJMMM International Journal of Minerals, Metallurgy and Materials 矿物冶金与材料学报（英文版）

# Effect of interaction of refractories with Ni-based superalloy on inclusions during vacuum induction melting

Xiao-yong Gao, Lin Zhang, Xuan-hui Qu, Xiao-wei Chen, and Yi-feng Luan

Cite this article as:
Xiao-yong Gao, Lin Zhang, Xuan-hui Qu, Xiao-wei Chen, and Yi-feng Luan, Effect of interaction of refractories with Ni-based superalloy on inclusions during vacuum induction melting, *Int. J. Miner. Metall. Mater.*, 27(2020), No. 11, pp. 1551-1559. https://doi.org/10.1007/s12613-020-2098-9



---

*International Journal of Minerals, Metallurgy and Materials*
*Volume 27, Number 11, November 2020, Page 1551*
**https://doi.org/10.1007/s12613-020-2098-9**

# Effect of interaction of refractories with Ni-based superalloy on inclusions during vacuum induction melting

*Xiao-yong Gao*[*], *Lin Zhang*[*], *Xuan-hui Qu*, *Xiao-wei Chen*, *and Yi-feng Luan*

Beijing Advanced Innovation Center for Materials Genome Engineering, Institute for Advanced Materials and Technology, University of Science and Technology Beijing, Beijing 100083, China
(Received: 20 January 2020; revised: 11 May 2020; accepted: 12 May 2020)

**Abstract:** This study documents laboratory-scale observation of the interactions between the Ni-based superalloy FGH4096 and refractories. Three different crucibles were tested—MgO, $Al_2O_3$, and MgO–spinel. We studied the variations in the compositions of the inclusions and the alloy–crucible interface with the reaction time using scanning electron microscopy equipped with energy dispersive X-ray spectroscopy and X-ray diffraction. The results showed that the MgO and MgO–spinel crucibles form MgO-containing inclusions (Al–Mg oxides and Al–Mg–Ti oxides), whereas the inclusions formed when using the $Al_2O_3$ crucible are $Al_2O_3$ and Al–Ti oxides. We observed a new $MgAl_2O_4$ phase at the inner wall of the MgO crucible, with the alloy melted in the MgO crucible exhibiting fewer inclusions. No new phase occurred at the inner wall of the $Al_2O_3$ crucible. We discuss the mechanism of interaction between the refractories and the Ni-based superalloy. Physical erosion was found to predominate in the $Al_2O_3$ crucible, whereas dissolution and chemical reactions dominated in the MgO crucible. No reaction was observed between three crucibles and the Ti of the melt although the Ti content (3.8wt%) was higher than that of Al (2.1wt%).

**Keywords:** FGH4096 superalloy; vacuum induction melting; crucible; inclusion; Mg/O ratio

## 1. Introduction

FGH4096 superalloy is among the most crucial powder-metallurgy turbine-disk superalloys used in aero-engineering because of its excellent rupture life, favorable creep resistance, and microstructural stability at high temperatures up to 923 K [1–5]. However, inclusions can degrade its mechanical properties (e.g., tensile strength, fatigue resistance) [6–7]. The inclusion issue is one of the most significant problems for ensuring the quality of superalloys. Typically, superalloys are compounds containing metals (aluminum, magnesium, titanium, calcium, cerium, etc.) and non-metallic elements (oxygen, sulfur, and nitrogen) [8–11]. Jiang *et al*. [7] found fatigue cracks to first nucleate within inclusions that are irregular in shape. Therefore, the inclusion issue is of considerable interest in the development of the FGH4096 superalloy. It is widely accepted that inclusions are mainly introduced during the primary melt process, i.e., vacuum induction melting (VIM).

VIM, the principal process used to manufacture the critical-rotating-component hardware of Ni-base superalloys, has served the aerospace industry well for decades [12–15]. The crucible material used has been a key issue during this time. Numerous studies have been conducted regarding various crucible materials, including $Al_2O_3$ [16–18], MgO, MgO–spinel, $Al_2O_3$–spinel, $Y_2O_3$ [19–20], $ZrO_2$ [21], and CaO [22–23]. Among them, CaO, $Y_2O_3$, and $ZrO_2$ have shown high thermochemical stability and low contamination during melting at high temperature. However, CaO is not suitable as a crucible in industrial furnaces because its sensitivity to humidity, and $Y_2O_3$ and $ZrO_2$ are very expensive for industrial-scale applications. Therefore, to date, MgO and $Al_2O_3$ remain the predominant components used in the manufacture of crucibles for VIM superalloys.

The relationship between the mechanical properties of FGH4096 superalloy and its inclusions has been extensively researched [1–3,6–7]. However, the formation mechanism of the inclusions in FGH4096 superalloy during VIM has rarely been addressed, so the formation and evolution of inclusions in FGH4096 superalloy during VIM must be further investigated.

*These authors contributed equally to this work.
Corresponding author: Lin Zhang E-mail: zlin@ustb.edu.cn

## 2. Experimental

### 2.1. Raw materials

Table 1 shows the designated chemical composition of FGH4096 superalloy, the raw materials of which were prepared in purities higher than 99.9%. We investigated three types of crucible materials (MgO, $Al_2O_3$ and MgO–spinel) in this study. The dimensions of the crucibles were 80 mm in outer diameter, 60 mm in inner diameter and 130 mm in inner height. The crucibles were composed of chemical reagents with a purity higher than 99%. The properties of the crucibles, as provided by the manufacturer, are shown in Table 2. The chemical compositions of the three types of crucibles were analyzed using an X-ray fluorescence spectrometer (XRF). All crucibles were produced using cold isostatic pressing and ordinary pressure sintering techniques to improve their resistances to thermal shock. The sizes of the ceramic particles ($Al_2O_3$, MgO) ranged between 0–1 mm.

**Table 1. Designated chemical composition of FGH4096 superalloy** wt%

| Cr | Co | Mo | W | Ti | Al | Nb | C | Ni |
|---|---|---|---|---|---|---|---|---|
| 15.0–16.5 | 12.5–13.5 | 3.8–4.2 | 3.8–4.2 | 3.5–3.9 | 2.0–2.4 | 0.6–1.0 | 0.02–0.05 | Bal. |

**Table 2. Properties of crucibles in current work**

| Crucible | MgO / wt% | $Al_2O_3$ / wt% | $SiO_2$ / wt% | $TiO_2$ / wt% | Porosity / % | Bulk density / ($kg·m^{-3}$) |
|---|---|---|---|---|---|---|
| MgO | 99.32 | 0.24 | 0.21 | 0.20 | 17.5 | $3.0\times10^3$ |
| $Al_2O_3$ | 0.09 | 99.64 | 0.10 | 0.11 | 17.0 | $2.9\times10^3$ |
| MgO–spinel | 85.68 | 13.39 | 0.44 | 0.41 | 17.2 | $3.7\times10^3$ |

### 2.2. Experimental procedure

A 2-kg-scale VIM furnace was utilized in the experiments. Fig. 1 shows a schematic of the experimental apparatus. A total of 1 kg of raw materials was used in each heat. As late additions, reactive elements (Al and Ti) were added to the melt through the hopper to prevent the formation of oxides and minimize the in-melt time for low-melting elements and thereby prevent burning off. First, the VIM chamber was evacuated to a vacuum degree of $1\times10^{-2}$ Pa and then backfilled with pure argon to 0.05 MPa before melting. Then, the furnace was heated to 1773 K at a rate of 25 K/min and maintained at 1773 K for 10 min to ensure homogenization prior to start time. The experimental times of each group of crucibles were 5, 10, 30, and 60 min, respectively. When an experiment was finished, the molten alloy was poured into a steel mold of diameter 40 mm. Table 3 lists the experimental conditions.

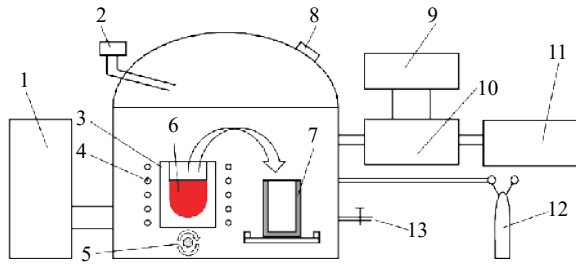


**Fig. 1. Schematic of experimental apparatus. 1—High frequency power supply; 2—Hopper; 3—Crucible; 4—Induction coil; 5—Rotating axis; 6—Molten alloy; 7—Steel mold; 8—Viewing window; 9—Pressure gage; 10—Diffusion pump; 11—Mechanical pump; 12—Ar gas; 13—Gas outlet.**

**Table 3. Experimental conditions and composition of FGH4096 superalloy for each heat**

| Heat No. | Crucible material | Melting time / min | Composition after experiments / wt% | | | |
|---|---|---|---|---|---|---|
| | | | Al | Ti | Mg | O |
| A1 | $Al_2O_3$ | 5 | 2.138 | 3.815 | <0.0001 | 0.0039 |
| A2 | $Al_2O_3$ | 10 | 2.137 | 3.815 | <0.0001 | 0.0037 |
| A3 | $Al_2O_3$ | 30 | 2.136 | 3.814 | <0.0001 | 0.0030 |
| A4 | $Al_2O_3$ | 60 | 2.137 | 3.815 | <0.0001 | 0.0041 |
| MS1 | MgO–spinel | 5 | 2.136 | 3.814 | 0.0002 | 0.0030 |
| MS2 | MgO–spinel | 10 | 2.135 | 3.815 | 0.0004 | 0.0028 |
| MS3 | MgO–spinel | 30 | 2.134 | 3.814 | 0.0007 | 0.0025 |
| MS4 | MgO–spinel | 60 | 2.134 | 3.814 | 0.0010 | 0.0030 |
| M1 | MgO | 5 | 2.134 | 3.815 | 0.0007 | 0.0023 |
| M2 | MgO | 10 | 2.132 | 3.814 | 0.0016 | 0.0015 |
| M3 | MgO | 30 | 2.131 | 3.814 | 0.0017 | 0.0019 |
| M4 | MgO | 60 | 2.130 | 3.814 | 0.0019 | 0.0016 |

### 2.3. Analysis

After VIM, we analyzed the O content by the LECO (TC-300 combustion analyzer) method, which uses NIST-certified standards with O values accurate to 0.0001wt%. The Al, Ti, and Mg contents in all the samples were determined using inductively coupled plasma-atomic emission spectroscopy (ICP-AES). The compositions of the inclusions of the metallographic samples were characterized using a scanning electron microscope (SEM) equipped with an energy dispersive spectrometer (EDS) with the acceleration voltage of 20 kV. The crucible samples were cut from the same location (10 mm below the liquid-alloy surface). The inner walls of the crucible samples were analyzed using X-ray diffraction (XRD). We also analyzed the interface of the crucible by SEM and EDS using map scanning.

## 3. Results and discussion

### 3.1. Inclusions in alloy

Based on their morphologies and chemical compositions, the inclusions can be classified into four types, namely, (1) $Al_2O_3$ oxides, (2) Al–Ti oxides, (3) Al–Mg oxides, and (4) Al–Mg–Ti oxides. Fig. 2 shows SEM images and the EDS results for these inclusion types. Table 4 shows the specifications of each type of inclusion.

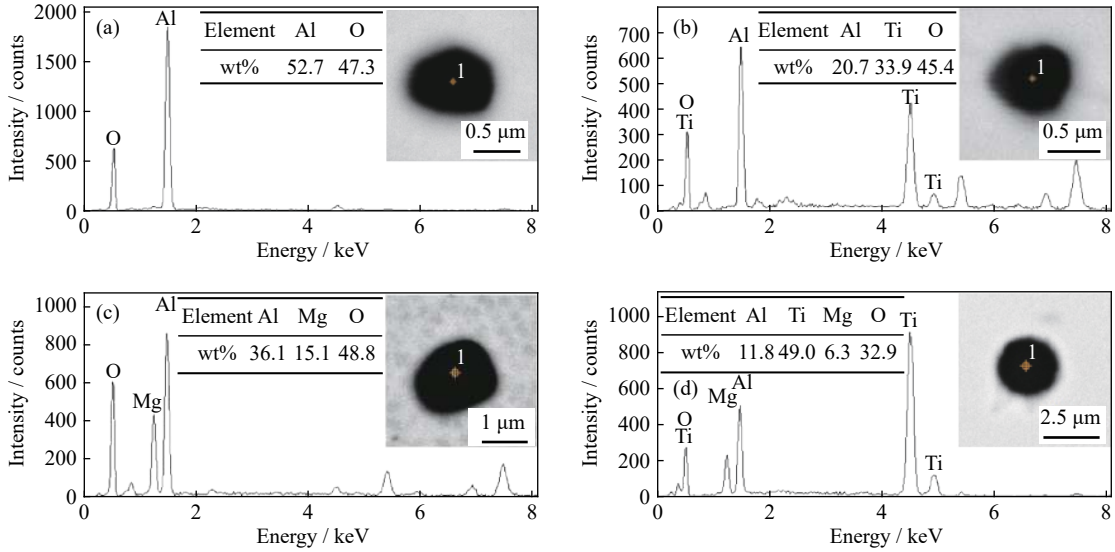


**Fig. 2. Morphology and EDS result of each type of inclusion: (a) type 1; (b) type 2; (c) type 3; (d) type 4.**

**Table 4. Types of oxide inclusion in different heats**

| Type | Specification of inclusions | Heats ($Al_2O_3$) | | | | Heats (MgO–spinel) | | | | Heats (MgO) | | | |
|---|---|---|---|---|---|---|---|---|---|---|---|---|---|
| | | A1 | A2 | A3 | A4 | MS1 | MS2 | MS3 | MS4 | M1 | M2 | M3 | M4 |
| 1 | $Al_2O_3$ | ×× | ×× | ×× | ×× | ×× | × | × | | × | | | |
| 2 | Al–Ti oxide | × | × | × | × | × | × | × | | × | | | |
| 3 | Al–Mg oxide | | | | | × | ×× | ×× | ×× | ×× | ×× | ×× | ×× |
| 4 | Al–Mg–Ti oxide | | | | | × | × | × | × | × | × | × | × |

Note: ××—Main type of inclusions; ×—Small amount of inclusions.

The inclusions in Heats A1–A4 were mainly $Al_2O_3$ with some minor Al–Ti oxide, and were mostly irregular in shape. Some were deoxidation products from the addition of Al and Ti. Others were crucible particles that had become detached because of the physical erosion of the melt under the electromagnetic stirring force. The compositions of the inclusions did not change as a function of the melting time, which suggests that almost no chemical reaction occurred between the alloy melt and the $Al_2O_3$ crucible. When the MgO–spinel crucible was applied, $Al_2O_3$ comprised the main inclusions at 5 min (Heat MS1), whereas nearly spherical Al–Mg oxides were the main inclusions after 10 min. When the MgO crucible was used, Al–Mg oxides were the main inclusions in Heats M1–M4. At 5 min, $Al_2O_3$, Al–Ti oxides, Al–Mg oxides, and Al–Mg–Ti oxides were all observed. At 10, 30, and 60 min, only Al–Mg oxides and Al–Mg–Ti oxides were observed, which indicates that the $Al_2O_3$ and Al–Ti oxides had been completely converted to MgO-containing oxides.

Fig. 3 shows the variation in the number densities of oxides with time, in which we can see that the number densities of the oxides in Heats M1–M4 are lower than those in Heats

A1–A4 and Heats MS1–MS4 at the same melting time. More inclusions are observed in Heats A1–A4. In addition, the amount of inclusions first decreases with time and then increases at 60 min in the cases of the $Al_2O_3$ and MgO–spinel crucibles, whereas in the case of the MgO crucible, the inclusions continue to decrease at 60 min. The fluid flow of the molten superalloy under electromagnetic force favors the floating of the inclusions to the top [24–26].

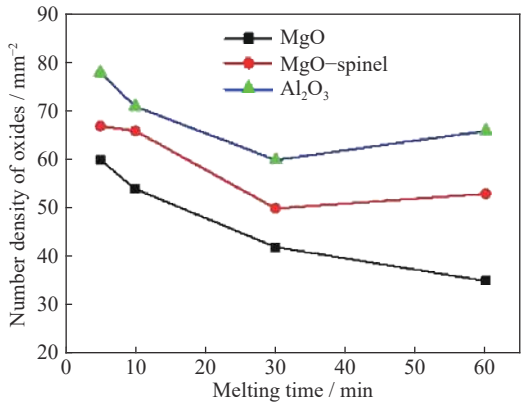


**Fig. 3. Variations in the number densities of oxides with time.**

### 3.2. Compositions of alloys and inclusions

Table 3 and Fig. 4 show the compositions of the alloys and inclusions, respectively. In Heats A1–A4, the Al, Ti, and Mg contents change only slightly with time. In Heats MS1–MS4 and Heats M1–M4, the Al contents decrease and the Mg contents increase with time, with the Ti contents changing very little. However, the Mg contents in the alloys in Heats M1–M4 are higher than those in Heats MS1–MS4 at the same melting time (see Fig. 4(a)). In the case of the MgO crucible, the Mg content increases sharply up to 10 min of reaction time and then increases slowly after 10 min of melting. The ratio of increase in the Mg content in Heats MS1–MS4 is nearly the same as that in Heats M1–M4 when the melting time is longer than 30 min, which suggests that they have nearly the same reaction rate. As shown in Fig. 4(b), in Heats A1–A4 and MS1–MS4, the O contents first decrease when the melting time is less than 30 min, and then increase at 60 min, similar to the variation in the number densities of the oxides in the superalloy. However, the O contents in Heats M1–M4 decrease with melting time in general. In addition, the O contents in Heats M1–M4 are lower than those in Heats A1–A4 and MS1–MS4 at all four melting times. Furthermore, Fig. 5 shows the Mg/O ratios in the superalloys and the MgO contents in the inclusions, in which we see that the Mg/O ratios in Heats M1–M4 are high, as are the MgO contents. It is interesting that the MgO contents in the inclusions linearly increase with the ratio of Mg/O in Heats MS1–MS4.

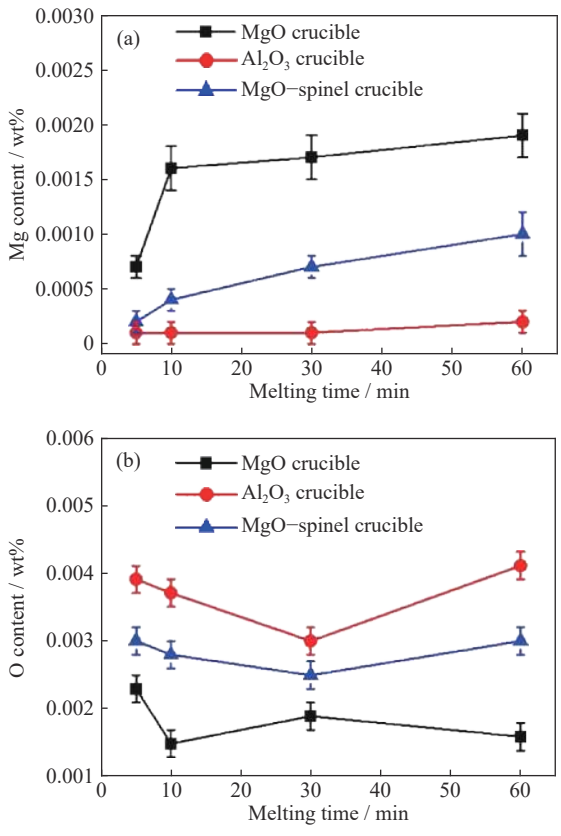


**Fig. 4. Mg and O contents after each heat.**

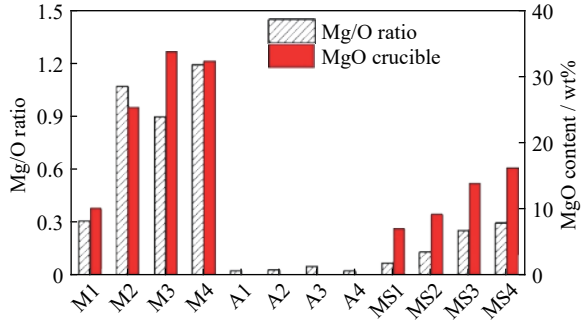


**Fig. 5. Mg/O ratio in alloys and MgO content in inclusions after each heat.**

### 3.3. Superalloy–crucible interface

Fig. 6(a) shows an elemental map of a cross section of the MgO crucible prior to VIM. After 5 min of reaction time, an Al band appears at the interface. Fig. 6(b) shows an elemental map of the MgO crucible after 60 min of reaction time, in which the Al band is clear and continuous. Studies [18,20–21] have indicated that the alloy–crucible reaction can generate solid or gaseous products, which may adhere to the crucible wall and hinder further reaction. Furthermore, our XRD results (see Fig. 7(a)) show that an $MgAl_2O_4$ phase occurs at the crucible walls, which suggests that the Al band is actually a $MgAl_2O_4$ layer. In addition, the thickness of the Al band of the MgO crucibles increases as a function of melt-

ing time, as shown in Fig. 8. The Al band is discontinuous in Heat M1, but more continuous in Heat M2. Continuous and thick Al bands are evident in Heats M3 and M4. All the above information regarding the MgO crucible indicates that MgO reacts with the FGH4096 superalloy melt. It is interesting that the inner wall of the MgO crucible becomes smooth after VIM, which is considered to be preferable. However, unlike the MgO crucibles described above, no new elemental enrichment is observed at the interface of the $Al_2O_3$ crucible after VIM, as shown in Fig. 9. The XRD results of the inner walls of the $Al_2O_3$ crucibles (Fig. 7(b)) further demonstrate that no new phase forms. Similar to the $Al_2O_3$ crucibles, no new elemental enrichment is observed at the inner walls of the MgO–spinel crucible after VIM, as shown in Fig. 10. Fig. 7(c) shows the XRD results for the inner walls of the MgO–spinel crucible. However, this does not mean that MgO–spinel does not react with the melt, because the reaction products $Al_2O_3$ and spinel have the same composition as they do in the crucible. It is difficult to distinguish between them.

Additionally, for all three groups of crucible samples, it is interesting to note that no Ti elemental enrichment was observed at the interface, although Ti was also active and its content (3.8wt%) was higher than Al (2.1wt%).

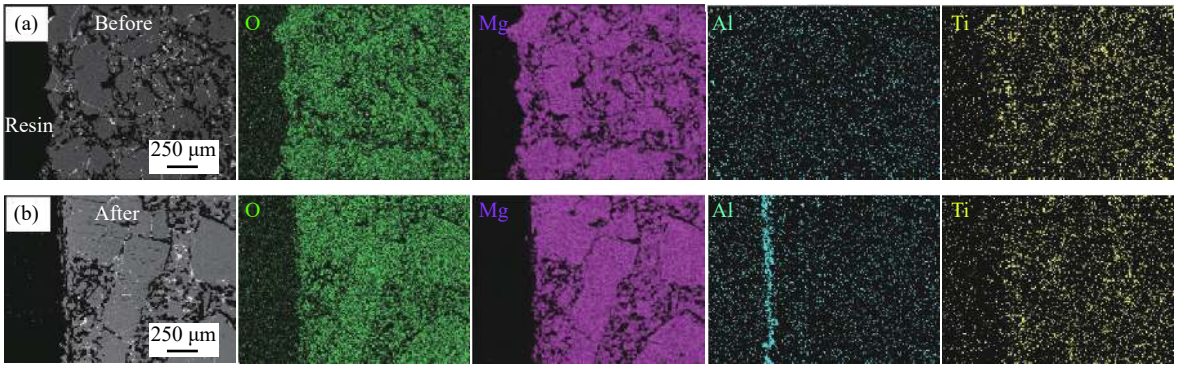


**Fig. 6. Elemental maps of MgO crucible interface: (a) before VIM; (b) after 60 min of VIM.**

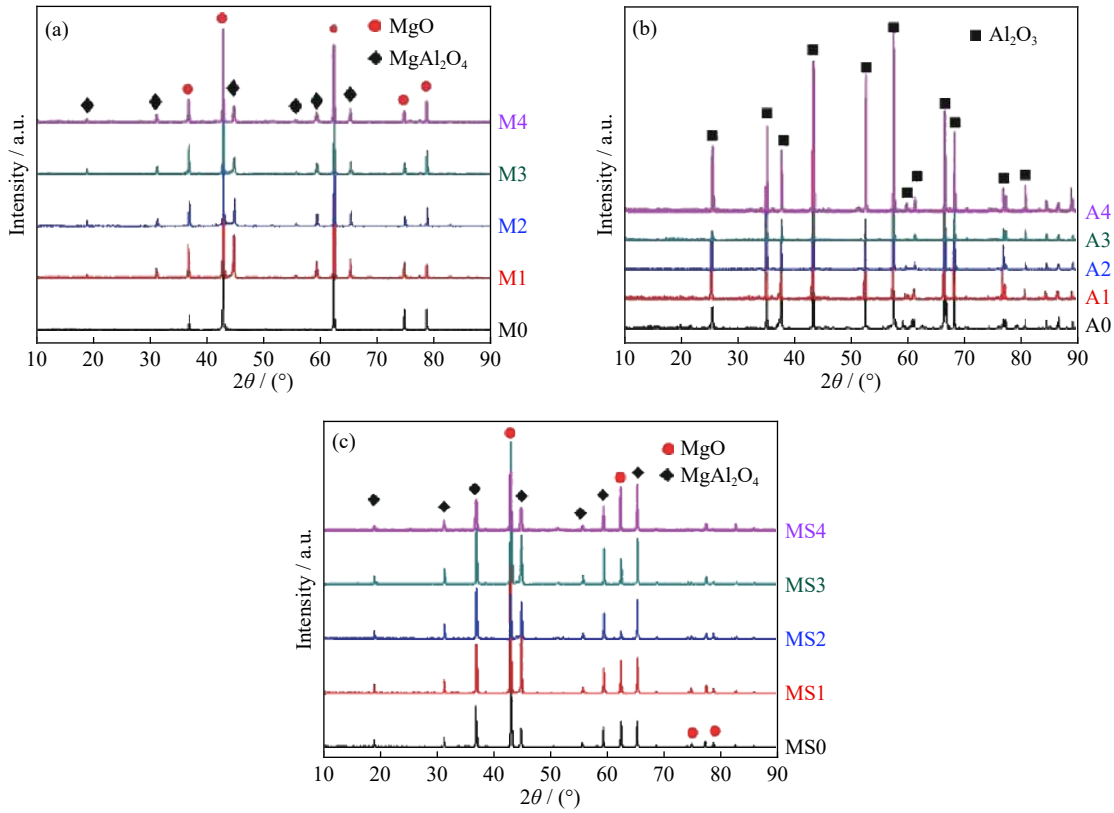


**Fig. 7. XRD spectra of inner walls of the three groups of crucibles: (a) MgO crucibles; (b) $Al_2O_3$ crucibles; (c) MgO–spinel crucibles.**

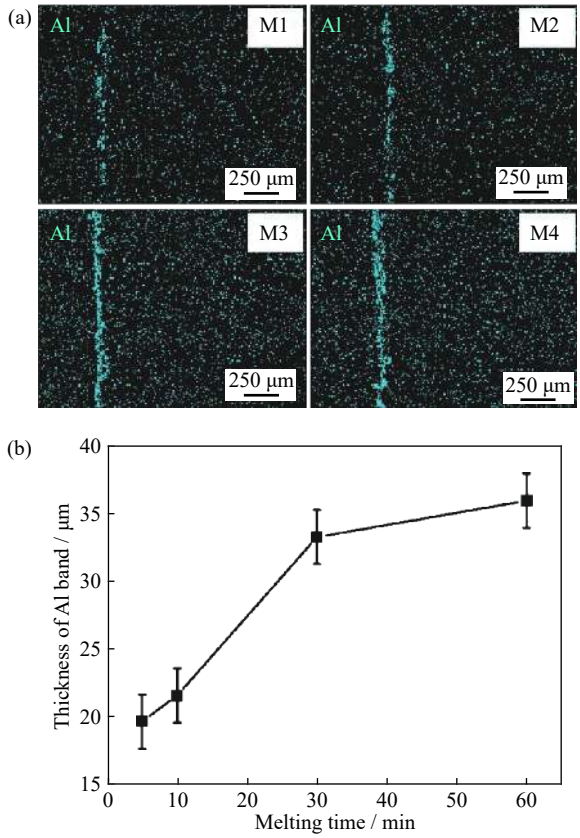


**Fig. 8. Maps and thicknesses of Al band at the interface of the MgO crucible with melting time.**

### 3.4. Mechanism of superalloy–crucible reaction

During the VIM process, the interaction between the crucible and alloy includes a dissolution reaction, chemical reaction, and physical erosion. In many cases, such as industrial production, the use of top slag cannot be fully avoided for economic reasons. The predominant reaction is that between the refractory and the liquid slag [27–28], which makes the interaction more complex. In the present study, to prevent its influence on the chemical composition of the superalloy and crucibles, we used no top slag.

In the dissolution reaction, Mg and Al might be introduced into the melt by the dissolution of their oxides (MgO and $Al_2O_3$, respectively), which can be expressed as shown in Eqs. (1) and (2).

$$MgO(s) = [O] + [Mg] \tag{1}$$

$$1/3Al_2O_3(s) = [O] + 2/3[Al] \tag{2}$$

for which the equilibrium constants become:

$$K_1 = \frac{\alpha_{Mg} \cdot \alpha_O}{\alpha_{MgO}} \tag{3}$$

$$K_2 = \frac{\alpha_{Al}^{2/3} \cdot \alpha_O}{\alpha_{Al_2O_3}^{1/3}} \tag{4}$$

Thus, if the activity product $\alpha_{Mg} \times \alpha_O$ in the alloy is less than $K_1$, Eq. (1) can proceed in the forward direction and MgO can dissolve in the superalloy. Of course, whether Eq.

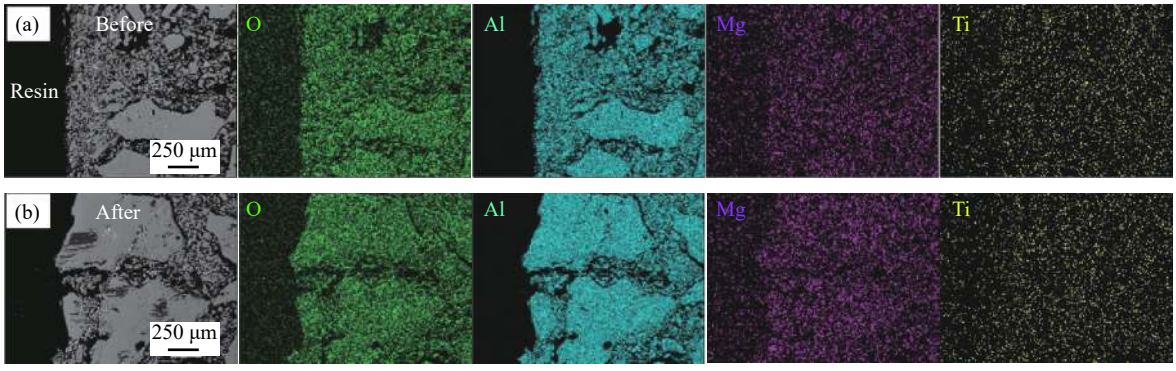


**Fig. 9. Elemental maps of $Al_2O_3$ crucible interface: (a) before VIM; (b) after 60 min of VIM.**

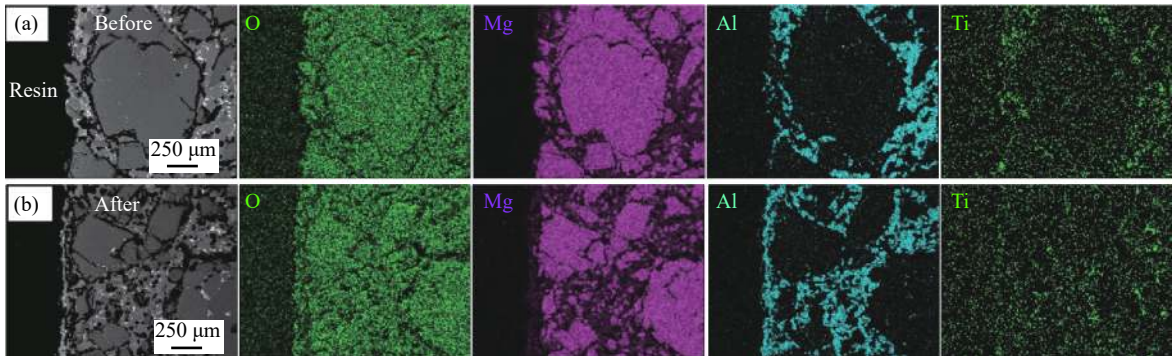


**Fig. 10. Elemental maps of MgO–spinel crucible interface: (a) before VIM; (b) after 60 min of VIM.**

(1) is feasible or not will depend on the solubility of Mg and oxygen in the superalloy and the kinetics of that dissolution. In the present study, the Mg content is very low, so Eq. (1) works. The $Al_2O_3$ crucible follows a similar rule, but the Al content is as high as 2.2wt%, which makes the dissolution of $Al_2O_3$ impossible. In other words, the dissolution of $Al_2O_3$ is very weak.

The chemical reaction between the MgO crucible and the superalloy has two stages, as shown in Fig. 11. In Stage 1, the MgO crucible reacts with the Al of the molten alloy, which can be expressed as shown in Eq. (5) [28]. This reaction generates dissolved Mg in the alloy and $Al_2O_3$, which adheres to the inner wall of the crucible to form an unstable $Al_2O_3$ layer. The formation of dissolved Mg plays a significant role in the evolution of the inclusions. Studies [29–31] have indicated that $Al_2O_3$ inclusions are not stable and transform into $MgAl_2O_4$ when dissolved Mg is present in the alloy melt. This phenomenon also occurs in Al–Ti oxide inclusions because the $Ti_2O_3$ of the inclusion is less stable than $Al_2O_3$. In Stage 2, $Al_2O_3$ reacts with the MgO of the crucible to form a stable $MgAl_2O_4$ spinel layer, as shown in Eq. (6). On the other hand, dissolved Mg can reduce the $Al_2O_3$ and $Ti_2O_3$ in the inclusions, which can be expressed as shown in Eqs. (7) [20,28] and (8), respectively. This modifies the composition of the inclusions such that the unstable $Al_2O_3$ and Al–Ti oxide inclusions are transformed into stable Al–Mg oxides.

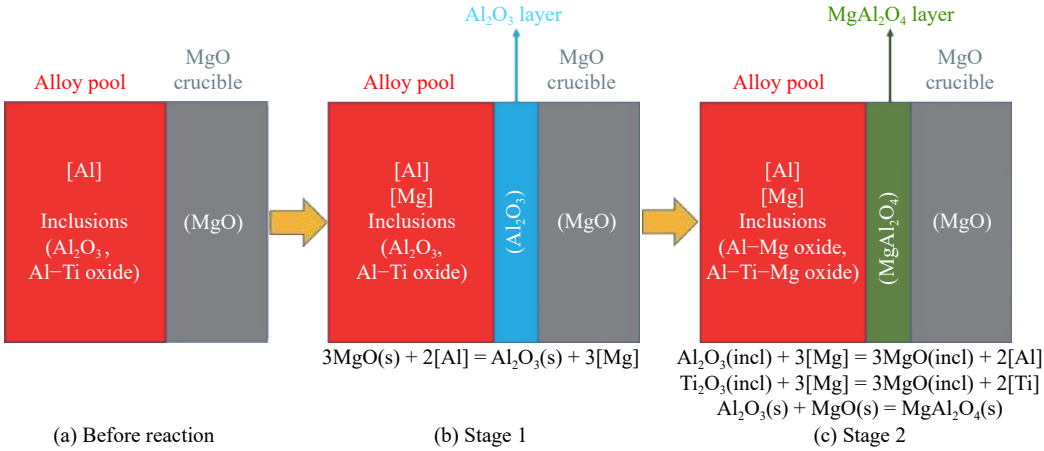


**Fig. 11. Schematic illustration of the superalloy–MgO crucible reaction mechanism during VIM.**

$$3MgO(s) + 2[Al] = Al_2O_3(s) + 3[Mg] \quad (5)$$

$$Al_2O_3(s) + MgO(s) = MgAl_2O_4(s) \quad (6)$$

$$4Al_2O_3(incl) + 3[Mg] = 3MgO \cdot Al_2O_3(incl) + 2[Al] \quad (7)$$

$$Ti_2O_3(incl) + 3[Mg] = 3MgO(incl) + 2[Ti] \quad (8)$$

where subscript "incl" is the abbreviation of inclusion. The mechanism of the chemical reaction between the MgO–spinel crucible and the superalloy is similar to that between the MgO crucible and the superalloy. However, the Mg contents in Heats MS1–MS4 are lower than those in Heats M1–M4 for the same melting times. This is due to the presence of spinel, which occupies a large proportion of the inner wall of the crucible and therefore hinders the chemical reaction between the Al of the alloy and the MgO of the crucible. However, we observed no chemical reaction between the $Al_2O_3$ crucible and the superalloy, which suggests that Ti does not react with the $Al_2O_3$ crucible because no reaction product forms at the interface.

In addition to the dissolution and chemical reactions, physical erosion occurs between the crucible and the melt [20]. In the VIM process, the electromagnetic stirring force applied to the surface causes relative movement between the melt and the crucible, which mechanically erodes the crucible. With continuous stirring, crucible particles become detached and disperse into the melt and a fresh crucible surface is then exposed to further erosion. Some of these detached crucible particles become dissolved in the melt, which contaminates the metal with oxygen. Others remain dispersed in the melt and float to the top surface due to the density difference between the melt and the oxide particles. In the present study, extensive detachment of $Al_2O_3$ crucible particles occurred in the melt because the inner surface had already become rough at 5 min, as shown in Fig. 12. This is why the oxygen content and number of inclusions increased after 30 min. However, the inner surface of the MgO crucible remained smooth even at 60 min. This is because the newly formed $MgAl_2O_4$ spinel layer can withstand erosion by high-temperature superalloy melt even if its thickness is just 36 μm at 60 min.

In summary, the dominant interaction between the $Al_2O_3$ crucible and the superalloy is physical erosion, whereas those of the MgO and MgO–spinel crucibles and the superalloy are the dissolution and chemical reactions. The MgO crucible is preferential when VIM is used with the FGH4096 superalloy because the $MgAl_2O_4$ layer that forms prevents contact between the MgO crucible and the superalloy and inhibits

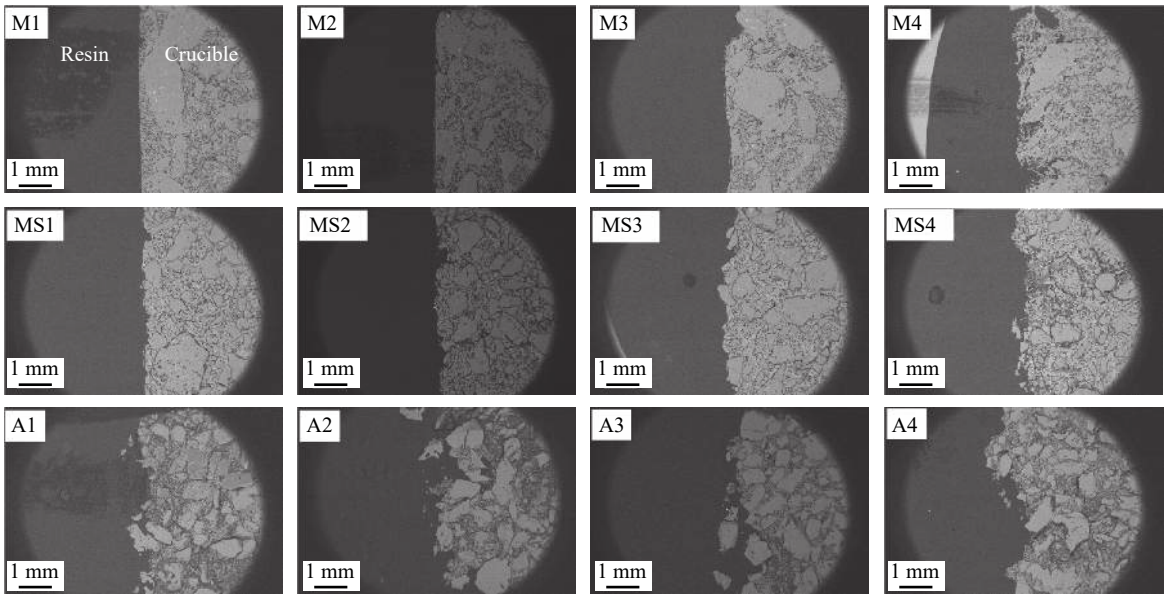


**Fig. 12. SEM images of superalloy–crucible interfaces.**

further erosion of the crucible.

## 4. Conclusions

In this paper, we described the results of our experimental melting of FGH4096 superalloy in a VIM furnace using three groups of crucibles and various melting times. Thermodynamic analysis was performed to confirm and explain the chemical reactions between the crucibles and the superalloy melt. The principal findings can be summarized as follows:

(1) The use of an MgO crucible has a great effect on the compositions of the superalloy and inclusions. The reaction between an MgO crucible and superalloy has two stages. The first stage is the reaction between the MgO of the crucible and the Al of the molten alloy, the products of which are dissolved Mg and $Al_2O_3$, which adheres to the wall of the crucible. As a result, the Mg content increases in the superalloy as a function of melting time. In the second stage, the dissolved Mg in the molten alloy reacts with the $Ti_2O_3$ and $Al_2O_3$ of the inclusions to produce MgO-containing oxide inclusions. The $Al_2O_3$ adhered to the inner wall of the crucible reacts with the MgO of the crucible to form a $MgAl_2O_4$ spinel layer. The Mg/O ratio of the alloy is high, as is the MgO content of the inclusions.

(2) Similar to the MgO crucible, the MgO–spinel crucible reacts with the Al of the melt and the Mg content increases. $Al_2O_3$ and Al–Ti oxides are converted into Al–Mg oxides and Al–Ti–Mg oxides, respectively. However, the Mg contents in Heats MS1–MS4 were lower than those in Heats M1–M4 at the same melting time. The MgO content of the inclusions were observed to linearly increase with the Mg/O ratio.

(3) The $Al_2O_3$ crucible was found to have almost no influence on the inclusions. The inclusions in Heats A1–A4 comprised $Al_2O_3$ plus a minor amount of Al–Ti oxides. The chemical compositions of the inclusions did not change with melting time.

(4) A relatively high Ti (3.8wt%) content in the superalloy melt did not react with the MgO, MgO–spinel, or $Al_2O_3$ crucibles.

(5) The MgO crucible exhibited a greater ability to resist physical erosion by the superalloy melt than the $Al_2O_3$ crucible.

## Acknowledgements

This work is financially supported by the Natural Science Foundation of China (No. 51974029), the Natural Science and Technology Major Project (No. 2017-VI-0014-0086), and Fundamental Research Funds for the Central Universities (Nos. FRF-AT-19-013 and FRF-NP-19-003).

## References

[1] Z.C. Peng, G.F. Tian, J. Jiang, M.Z. Li, Y. Chen, J.W. Zou, and F.P.E. Dunne, Mechanistic behaviour and modelling of creep in powder metallurgy FGH96 nickel superalloy, *Mater. Sci. Eng. A*, 676(2016), p. 441.

[2] M.J. Zhang, F.G. Li, B. Chen, and S.Y. Wang, Investigation of micro-indentation characteristics of PM nickel-base superalloy FGH96 using dislocation-power theory, *Mater. Sci. Eng. A*, 535(2012), p. 170.

[3] D.D. Yang, Y. Shi, G.L. Miao, X.G. Yang, and D.Q. Shi, The study of the relationship between life limiting factor and stress level for FGH96, *MATEC Web Conf.*, 165(2018), p. 22031.

[4] B. Fang, G.F. Tian, Z. Ji, M.Y. Wang, C.C. Jia, and S.W. Yang, Study on the thermal deformation behavior and microstructure of FGH96 heat extrusion alloy during two-pass hot deformation, *Int. J. Miner. Metall. Mater.*, 26(2019), No. 5, p. 657.

[5] Y.F. Feng, X.M. Zhou, J.W. Zou, and G.F. Tian, Effect of cooling rate during quenching on the microstructure and creep property of nickel-based superalloy FGH96, *Int. J. Miner. Metall. Mater.*, 26(2019), No. 4, p. 493.

[6] G.L. Miao, X.G. Yang, and D.Q. Shi, Competing fatigue failure behaviors of Ni-based superalloy FGH96 at elevated temperature, *Mater. Sci. Eng. A*, 668(2016), p. 66.

[7] J. Jiang, J. Yang, T.T. Zhang, F.P.E. Dunne, and T.B. Britton, On the mechanistic basis of fatigue crack nucleation in Ni superalloy containing inclusions using high resolution electron backscatter diffraction, *Acta Mater.*, 97(2015), p. 367.

[8] M.H. Manjili and M. Halali, Removal of non-metallic inclusions from nickel base superalloys by electromagnetic levitation melting in a slag, *Metall. Mater. Trans. B*, 49(2018), No. 1, p. 61.

[9] J.D. Busch, J. Debarbadillo, and M. Krane, Flux entrapment and titanium nitride defects in electroslag remelting of INCOLOY alloys 800 and 825, *Metall. Mater. Trans. A*, 44(2013), No. 12, p. 5295.

[10] X.C. Chen, C.B. Shi, H.J. Guo, F. Wang, H. Ren, and D. Feng, Investigation of oxide inclusions and primary carbonitrides in Inconel 718 superalloy refined through electroslag remelting process, *Metall. Mater. Trans. B*, 43(2012), No. 6, p. 1596.

[11] H.E.O. Kellner, A.V. Karasev, O. Sundqvist, A. Memarpour, and P.G. Jönsson, Estimation of non-metallic inclusions in industrial Ni based alloys 825, *Steel Res. Int.*, 88(2017), No. 4, p. 1.

[12] R. Kennedy, R.M.F. Jones, R.M. Davis, M.G. Benz, and W.T. Carter, Superalloys made by conventional vacuum melting and a novel spray forming process, *Vacuum*, 47(1996), No. 6-8, p. 819.

[13] A. Choudhury, State of the art of superalloy production for aerospace and other application using VIM-VAR or VIM-ESR, *ISIJ Int.*, 32(1992), No. 5, p. 563.

[14] N. Nayan, Govind, C.N. Saikrishna, K.V. Ramaiah, S.K. Bhaumik, K.S. Nair, and M.C. Mittal, Vacuum induction melting of NiTi shape memory alloys in graphite crucible, *Mater. Sci. Eng. A*, 465(2007), No. 1-2, p. 44.

[15] Z.H. Zhang, J. Frenzel, K. Neuking, and G. Eggeler, On the reaction between NiTi melts and crucible graphite during vacuum induction melting of NiTi shape memory alloys, *Acta Mater.*, 53(2005), No. 14, p. 3971.

[16] H.X. Ji, S. Jones, and P.M. Marquis, Characterization of the interaction between molten titanium alloy and $Al_2O_3$, *J. Mater. Sci.*, 30(1995), No. 22, p. 5617.

[17] M. Koyama, S. Arai, S. Suenaga, and M. Nakahashi, Interfacial reactions between titanium film and single crystal α-$Al_2O_3$, *J. Mater. Sci.*, 28(1993), No. 3, p. 830.

[18] A. Misra, Reaction of Ti and Ti–Al alloys with alumina, *Metall. Trans. A*, 22(1991), No. 3, p. 715.

[19] Q.L. Li, H.R. Zhang, M. Gao, J.P. Li, T.X. Tao, and H. Zhang, Mechanisms of reactive element Y on the purification of K4169 superalloy during vacuum induction melting, *Int. J. Miner. Metall. Mater.*, 25(2018), No. 6, p. 696.

[20] R.J. Cui, M. Gao, H. Zhang, and S.K. Gong, Interactions between TiAl alloys and yttria refractory material in casting process, *J. Mater. Process. Technol.*, 210(2010), No. 9, p. 1190.

[21] K.F. Lin and C.C. Lin, Interfacial reactions between Ti–6Al–4V alloy and zirconia mold during casting, *J. Mater. Sci.*, 34(1999), No. 23, p. 5899.

[22] T. Degawa and T. Ototani, Refining of high purity Ni-base superalloy using calcia refractory, *Tetsu-to-Hagane*, 73(1987), No. 14, p. 1691.

[23] J.P. Niu, X.F. Sun, T. Jin, K.N. Yang, H.R. Guan, and Z.Q. Hu, Investigation into deoxidation during vacuum induction melting refining of nickel base superalloy using CaO crucible, *Mater. Sci. Technol.*, 19(2003), No. 4, p. 435.

[24] N. Verma, P.C. Pistorius, R.J. Fruehan, M. Potter, M. Lind, and S. Story, Transient inclusion evolution during modification of alumina inclusions by calcium in liquid steel: Part I. Background, experimental techniques and analysis methods, *Metall. Mater. Trans. B*, 42(2011), No. 4, p. 711.

[25] C. Wang, N.T. Nuhfer, and S. Sridhar, Transient behavior of inclusion chemistry, shape, and structure in Fe–Al–Ti–O melts: Effect of titanium source and laboratory deoxidation simulation, *Metall. Mater. Trans. B*, 40(2009), No. 6, p. 1005.

[26] Y.J. Kwon, J. Choi, and S. Sridhar, The morphology and chemistry evolution of inclusions in Fe–Si–Al–O melts, *Metall. Mater. Trans. B*, 42(2011), No. 4, p. 814.

[27] W.L. Wang, L.W. Xue, T.S. Zhang, L.J. Zhou, J.Y. Chen, and Z.H. Pan, Thermodynamic corrosion behavior of $Al_2O_3$, $ZrO_2$ hand MgO refractories in contact with high basicity slag, *Ceram. Int.*, 45(2019), No. 16, p. 20664.

[28] H.Y. Mu, T.S. Zhang, R. Fruehan, and B. Webler, Reduction of CaO and MgO slag components by Al in liquid Fe, *Metall. Mater. Trans. B*, 49(2018), No. 4, p. 1665.

[29] Z.Y. Deng and M.Y. Zhu, Evolution mechanism of non-metallic inclusions in Al-killed alloyed steel during secondary refining process, *ISIJ Int.*, 53(2013), No. 3, p. 450.

[30] M. Jiang, X.H. Wang, and W.J. Wang, Control of non-metallic inclusions by slag-metal reactions for high strength alloying steels, *Steel Res. Int.*, 81(2010), No. 9, p. 759.

[31] S.J. Luo, Y.H.F. Su, M.J. Lu, and J.C. Kuo, EBSD analysis of magnesium addition on inclusion formation in SS400 structural steel, *Mater. Charact.*, 82(2013), p. 103.